Probing the Martian atmospheric boundary layer using impact-generated seismo-acoustic signals

Marouchka Froment[1,2,3], Zongbo Xu[1], Philippe H. Lognonné[1], Carène Larmat[2], Raphael F. Garcia[4], Mélanie Drilleau[4], Brent G Delbridge[2], Aymeric Spiga[5], Taichi Kawamura[1], Éric Beucler[6,7]

[1]Université Paris Cité, Institut de physique du globe de Paris, CNRS, F-75005 Paris, France

[2]Earth and Environmental Sciences Division, Los Alamos National Laboratory, Los Alamos, NM 87545, USA

[3]NORSAR, Kjeller, Norway

[4]Institut Supérieur de l'Aéronautique et de l'Espace (ISAE-SUPAERO), Université de Toulouse, 31400 Toulouse, France

[5]Laboratoire de Météorologie Dynamique/Institut Pierre-Simon Laplace (LMD/IPSL), CNRS, Sorbonne Université, Paris, France

[6]Nantes Université, Université Angers, Le Mans Université, CNRS, UMR 6112, Laboratoire de Planétologie et Géosciences, F-44000 Nantes, France

[7]Nantes Université, UGE, Univ Angers, CNAM, CNRS, UAR 3281, Observatoire des sciences de l'univers Nantes Atlantique, F-44000 Nantes, France

Key Points:

- InSight recorded impact-generated infrasound on Mars. Their group velocity is sensitive to the structure of the atmospheric boundary layer.
- We conduct a Bayesian inversion of effective sound speed profiles with altitude based on group velocities measured for three impact events.
- The inverted profiles provide an indirect measurement of the Martian boundary layer, and validate models of the Mars Climate Database.

Corresponding author: Marouchka Froment, `mfroment@ipgp.fr`

Abstract

The properties of the first kilometers of the Martian atmospheric Planetary Boundary Layer have until now been measured by only a few instruments and probes. InSight offers an opportunity to investigate this region through seismoacoustics. On six occasions, its seismometers recorded short low-frequency waveforms, with clear dispersion between 0.4 and 4Hz. These signals are the air-to-ground coupling of impact-generated infrasound, which propagated in an low-altitude atmospheric waveguide. Their group velocity depends on the structure of effective sound speed in the boundary layer. Here, we conduct a Bayesian inversion of effective sound speed up to 2000m altitude using the group velocity measured for events S0981c, S0986c and S1034a. The inverted effective sound speed profiles are in good agreement with estimates provided by the Mars Climate Database. Differences between inverted and modeled profiles can be attributed to a local wind variation in the impact→station direction, of amplitude smaller than 2m/s.

Plain Language Summary

The Martian Planetary Boundary Layer corresponds to the first few kilometers of the atmosphere. The InSight lander offers the opportunity to investigate its properties via the coupling of seismic and acoustic waves. Impact-generated infrasound waves were recorded for the first time on Mars by the seismometers of the InSight mission. These infrasound waves propagated in an atmospheric waveguide in the first kilometers above the Martian surface, and thus present a frequency-dependent group velocity. This frequency-dependence, also known as a dispersion relation, is influenced by the structure of the speed of sound in the waveguide. Here, we use group velocity measured for events S0981c, S0986c and S1034a to invert the variations of effective sound speed between 0 and 2000 m altitude. For the three events, the inverted profiles are in good agreement with estimates provided by the Mars Climate Database using global climate modeling. The differences between inverted and modeled profiles can be attributed to a local variation in wind in the impact→station direction, with magnitude smaller than 2 m/s.

1 Introduction

The Planetary Boundary Layer (PBL) defines the region where the atmosphere of a planet interacts with the surface, through exchanges of momentum, heat and molecular species. On Mars, it extends from the surface up to about 10 km altitude, and it is also a

critical environment where landers, rovers and airborne spacecrafts operate (Petrosyan et al., 2011). In the Martian PBL, temperature undergoes significant daily variations, of about 50 to 80 K in amplitude at surface levels. The bottom of the PBL shows a superadiabatic lapse rate in the daytime, i.e., a negative temperature gradient with altitude, leading to instabilities and convective turbulences. Conversely, the temperature gradient reverses at night and becomes strongly stable. Capturing these phenomena is key to designing accurate models of the Martian climate, such as General Circulation Models (GCMs) (see e.g., Forget et al. (1999), Moudden and McConnell (2005), Segschneider et al. (2005), Takahashi et al. (2006)). At high altitudes ($\gtrsim$ 1 km), GCMs validate their results using orbiter data, and results at the surface level are validated using measurements from landers and rovers (Forget et al., 2001, 2014). However, data remains sparse at intermediate altitude including in most of the PBL (Petrosyan et al., 2011). Its properties have been sampled or inferred during entry, descent and landing of the Viking, InSight and Perseverance spacecrafts (Seiff & Kirk, 1977; Banfield et al., 2020; Paton et al., 2024). Temperature profiles up to 2 km altitude have notably been obtained by the Miniature Thermal Emission Spectrometer (Mini-TES) onboard Spirit and Opportunity, but these measurements were mostly limited to the late morning to the afternoon due to operational constraints (Smith et al., 2006; Mason & Smith, 2021).

The NASA InSight mission offers a new opportunity for atmospheric science on Mars. The lander operated a seismometer, the SEIS instrument, supported by a meteorological sensor suite (APSS) between 2018 and 2022 on Elysium Planitia (Banfield et al., 2018; Lognonné et al., 2019). Over the course of the mission, more than a thousand seismic events of tectonic, but also of atmospheric origin were captured by SEIS (Banerdt et al., 2020; InSight Marsquake Service, 2023; Ceylan et al., 2022). While some of these atmospheric events are produced by local perturbations, other are the seismic response to pressure excitations having propagated for a large distance through the Martian atmosphere.

On sols 533, 793, 981, 986, 1034 and 1160, which denote the number of Martian days after the landing of InSight, SEIS recorded six short dispersed low-frequency signals, with energy between 0.4 and 4 Hz (Garcia et al., 2022; Daubar et al., 2023). Each of them was preceded by a Very-high frequency (VF) seismic event, i.e., a type of marsquakes containing seismic energy above 2.4Hz and up to 10Hz and higher. Using a combination of seismic analysis and orbital imaging, Garcia et al. (2022) showed that both the VF and the dispersed arrivals originated from meteorite impacts. Precisely, the VF events are seismic waves

directly generated by impact cratering, while the subsequent dispersed arrivals are due to the air-to-ground coupling of the impact blast wave traveling through the Martian atmosphere. The location of the source of both the seismic and the seismo-acoustic signals is known thanks to orbital imaging of the craters.

The dispersion of these signals can be well explained by the presence of an atmospheric waveguide at low altitudes. On Earth, dispersed infrasound waves were recorded following surface explosions in the presence of such waveguide (Herrin et al., 2006; Negraru & Herrin, 2009; Schneider et al., 2018). Likewise on Mars, a waveguide may exist at night due to the rapid radiative cooling of the surface, and can be enhanced by favorable seasonal wind conditions (Garcia et al., 2017; Daubar et al., 2018). Waves traveling in such waveguides are referred to as "guided waves" and may propagate over large distances (Martire et al., 2020). Low-altitude guided waves interact with the surface, and thus excite ground deformation via compliance effects (Sorrells, 1971; Ben-Menahem & Singh, 2012). Xu et al. (2022) propose an analytical representation of Martian seismo-acoustic signals. They develop a 1D model for infrasound wave propagation and dispersion in a layered atmospheric waveguide, including their coupling through ground compliance (Xu & Lognonné, 2024; Tanimoto & Wang, 2019), yielding synthetic dispersed seismic signals at InSight's location.

The speed of sound in the Martian PBL defines the waveguide structure and governs infrasound propagation. In this previous work, the waveguide properties are estimated using models of the atmosphere of Mars provided by the Mars Climate Database (MCD) (Forget et al., 1999; Millour et al., 2015, 2018) at the time and place of various InSight events. The MCD interpolates meteorological fields, such as atmospheric temperature, density, pressure and wind, in time and space, based on grided outputs from GCMs. With limited alteration to the MCD models,Garcia et al. (2022) and Xu et al. (2022) obtain a good fit between synthetic waveforms and the dispersed signals recorded by InSight during events S0981c and S0986c. This result shows that we can extract further information on the Martian PBL and test MCD models using impact infrasound data.

In this study, we propose to invert profiles of the speed of sound up to 2 km above the surface of Mars from InSight dispersed seismo-acoustic signals, based on Xu et al. (2022)'s model for infrasound group velocities. We first describe this model and the sensitivity of group velocity to atmospheric structure. Then, we present the inversion method and its application to three seismic events (S0981c, S0986c and S1034a). The resulting atmospheric

models are compared to MCD predictions at InSight location at the time of each event to validate results of climate modeling in the PBL.

2 Analytical model of ground-coupled guided infrasound

We provide a brief description of the analytical model of coupled guided infrasound. We refer the reader to Xu et al. (2022) for further details.

2.1 Waveform model

The synthetic waveform is represented in the frequency domain, as a function of pulsation ω. We adopt the formalism of Xu et al. (2022) and express the velocity in the upward vertical direction, $u_z(\omega)$. The source, i.e. the impact crater, is located at distance x from the receiver. $u_z(\omega)$ is defined as follows:

$$u_z(\omega) = S(\omega)\exp\left(-ikx - ax\right)\frac{\exp\left(-i\pi/4\right)}{\sqrt{kx\pi/2}}\frac{P^2(\omega,0)}{\int P^2(\omega,z)dz}C_z(\omega). \tag{1}$$

In this expression, $S(\omega)$ is the spectrum of the impact blast source. C_z is the vertical compliance (see Xu et al. (2022) for details), and a is the attenuation of the Martian atmosphere. $P(\omega, z)$ is the *pressure eigenfunction*, quantifying the altitude range at which a pressure wave with pulsation ω is effectively trapped. The factor $\exp\left(-i\pi/4\right)/\sqrt{kx\pi/2}$ is a correction to account for the effects of geometrical spreading on the 1D wave model.

The dispersion is caused by a frequency-dependent wave number k and group velocity $v_g(\omega) = d\omega/dk$. In the above model, the dispersion is not affected by compliance and is solely due to the propagation of the infrasound wave in a refractive atmosphere, showing an increase in the medium propagation velocity, or acoustic impedance, with altitude. Therefore, the group velocity of the guided infrasound can be obtained directly from the ground deformation induced by pressure waves, i.e., from the seismic signal (Garcia et al., 2022).

The propagation velocity for infrasound depends on both the local temperature T and wind speed vector $\boldsymbol{w}$. They have an effective sound speed $\alpha_{\text{eff}} = \alpha_{\text{T}}(T) + \boldsymbol{w}\cdot\frac{\boldsymbol{k}}{\|\boldsymbol{k}\|}$, which is enhanced parallel to the wind direction. Hence, the structure of this effective sound speed in the atmosphere determines the group velocity in our model. Following Xu et al. (2022), we consider an invariant atmosphere in the propagation direction, and we represent its vertical variation through a succession of N layers, with layer n of thickness H_n having a constant effective sound speed $\alpha(z) = \alpha_n$ for $z \in [z_n, z_n + H_n]$, and a density ρ_n. The group velocity

can then be computed using a propagator matrix method (Aki & Richards, 2002) and a root finding algorithm (Xu et al., 2022).

2.2 Model sensitivity and parametrization

We assess the possibility of inverting the Martian atmospheric structure from the group velocities of coupled impact seismic signals. Parametric studies are performed to determine the sensitivity of v_g to variations of effective sound speed and density. This parametric study is detailed in section 2 of the Supporting Information (SI) and shows that group velocity is considerably more sensitive to variations in effective sound speed than in density. Moreover, v_g is more sensitive to changes in α_n at low altitude.

This parametric study confirms that an atmospheric sound speed profile formed by several layers and a half-space can be inverted from chirp group velocity. The structure of the waveguide depends on both the amplitude of α_n and the height H_n of each layer. On the other hand, the density within each layer can be fixed to values matching MCD models.

3 Methods

4 Data selection

Among the six impact events, only three present a high signal to noise ratio (SNR) and unambiguous group velocity recording: chirps of S0986c, S0981c and S1034a are chosen for this inversion. We point out that event S0986c present three distinct acoustic arrivals, labeled A1, A2 and A3 in Garcia et al. (2022). Garcia et al. interpret the strongest signal, A3, as being produced by the impact with known source location, while earlier ones are related to the entry and disruption of the associated meteoroid.

The properties of the three selected events (S0981c, S0986c A3 and S1034a) are summarized in Table 1. Their group velocity curve and their uncertainties are measured using the method described in Gaudot et al. (2021) (see also section 1 of the SI), and are shown on Fig. 1.

4.1 Bayesian Inversion design and tests

To quantify the uncertainty of each atmospheric models, a Bayesian inversion method is favored. In this study, the Markov chain Monte Carlo method is chosen (Geyer, 1991),

Table 1. Known properties of the three events selected for inversion, obtained from seismic analysis, from satellite imaging (see Garcia et al. (2022), Daubar et al. (2023) and from the InSight event catalog (InSight Marsquake Service, 2023)). Note that the distance of S0981c was reevaluated in Daubar et al. (2023).

Event	S0981c	S0986c A3	S1034a
Properties from seismic signal			
UTC Date (at event start time)	31 August 2021	5 September 2021	23 October 2021
UTC Time (at event start time)	04:04:01.00	05:23:58.00	18:26:43.00
Properties from orbital imaging			
Crater diameter (type) (m)	7.24 (single)	6.1 (cluster)	9.2 (single)
Crater latitude (°N)	0.397	3.974	3.866
Crater longitude (°E)	135.688	136.963	135.107
Distance to InSight (km)	240.6	85.1	48.4
Back azimuth (°)	179.2	111.6	219
Relevant time information			
Estimated UTC origin/impact time	4:03:13	5:23:44	18:26:30
Solar Longitude L_s	92.6	94.8	116.8
Local True Solar Time (LTST, hours)	23.2	21.3	3.3

in combination with a Parallel Tempering technique, to ensure that potential multimodal distributions of probability can be explored (Sambridge, 2014).

The propagation medium is a layered atmosphere, parameterized by layer heights H_n and effective sound speeds α_n in each layer and in the top halfspace. The number N of layers below the halfspace is also an important choice in the inversion. To avoid overfitting the group velocity curves, the influence of the number of layers on the model misfit was measured and is detailed in section 3 of the SI. No significant improvement of the misfit is obtained above $N = 4$, which is consequently chosen for all the subsequent inversions.

A uniform prior distribution is chosen for all the inverted parameters, with upper and lower bounds based on realistic values. The analysis of Garcia et al. (2017) shows that speed of sound may increase up to 2 km altitude in the Martian nocturnal boundary layer

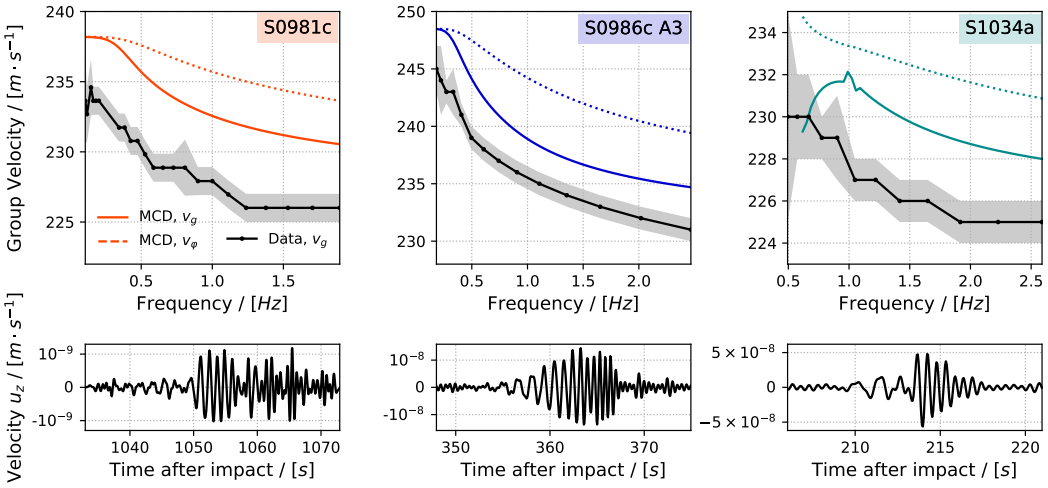

Figure 1. (top) Group velocity $v_g(\omega)$ measured for the dispersed arrivals of events S0981c, S0986c and S1034a. The uncertainty of group velocity measurements is represented in gray. The group velocity v_g predicted from MCD atmospheric profiles on the day on each event is also displayed in plain colored lines, and the predicted phase velocity v_φ with dashed colored lines. (bottom) Vertical ground velocity $u_z(t)$ of the recorded dispersed arrivals, bandpass-filtered between 0.5 and 2 Hz.

for solar longitudes $L_s \approx 90 - 100$ similar to our three events (i.e., summer in the northern hemisphere). Consequently, each layer thickness is picked within $[5, 400]$ m, for a total possible height of 1600 m initiating the halfspace. Effective sound speed takes values within $\alpha_0 \in [220, 240]$ m/s in the first layer. Starting from the third layer, variations of effective sound speed $\Delta\alpha = \alpha_n - \alpha_{n-1}$ are allowed within $[-5, 15]$ m/s. Negative variations in sound speeds are not allowed in the second layer above the surface, as this would result in a very poor waveguide.

An in-house implementation of the McMC and parallel tempering method is used. Tests of this method with synthetic atmospheric models and synthetic group velocity curves are presented in section 3 of the SI. They show that the inversion provides a satisfactory fit to the provided group velocity curves and initial atmospheric model.

5 Atmospheric Inversion Results

5.1 Effective sound speed profiles

The posterior distribution of group and phase velocity curves inverted for S0981c are shown on the right of Fig. 2. The inverted models provide a good fit to the data within the uncertainty of group velocity measurements. Similar figures for S0986c and S1034a are shown in section 4 of the SI. The three left panels of Fig. 2 show the posterior PDFs of effective sound speed profiles inverted from the group velocity curves of each event. These PDF are constructed from a distribution of 4-layer models which require sharp increase in velocity in the atmosphere. However, we note that a smoother model passing through the region of high probability density, here shown in blue, also provides a good fit to S0981c's group velocities. This confirms that the choice of a "staircase" model is not bringing unrealistic constraints to the inversion: instead, it captures the average effective sound speed between two bounds in altitude. The width of the posterior PDF is driven by model sensitivity and data uncertainty. Close to the surface, α_{eff} appears to be well constrained, within ± 1 m/s. However, the distribution of models becomes more spread out at higher altitude, especially for S1034a for which α_{eff} takes values between ~ 230 and ~ 245 m/s above 250 m altitude. This variation is of the same order as the prior distribution, displayed in section 4 of the SI, which means that the group velocity data of this event does not provide sufficient information to constrain effective sound speed at higher altitudes. At 500 m altitude, the region of high probability has a width of about 4 m/s for S0981c and 6 m/s for S0986c.

Our current objective is to compare atmospheric profiles inverted from impact infrasound to current models of the atmosphere using outputs of the Mars Climate Database. However, the resolution of MCD outputs is limited by the resolution of the GCM grids over which its interpolation is performed.

To ensure a meaningful comparison between inversion results and the MCD, we estimate a range of possible variations for wind, thermodynamical and effective sound speed during each event. To this aim, we query the database at a range of location covering the approximate area of a GCM grid cell around InSight. This is done at the time of the event, but also one Martian hour before and after to match the database temporal resolution. We thus establish the minimum and maximum values of parameters based on which spatial and temporal interpolation is performed (see Fig. S10 of the SI for details).

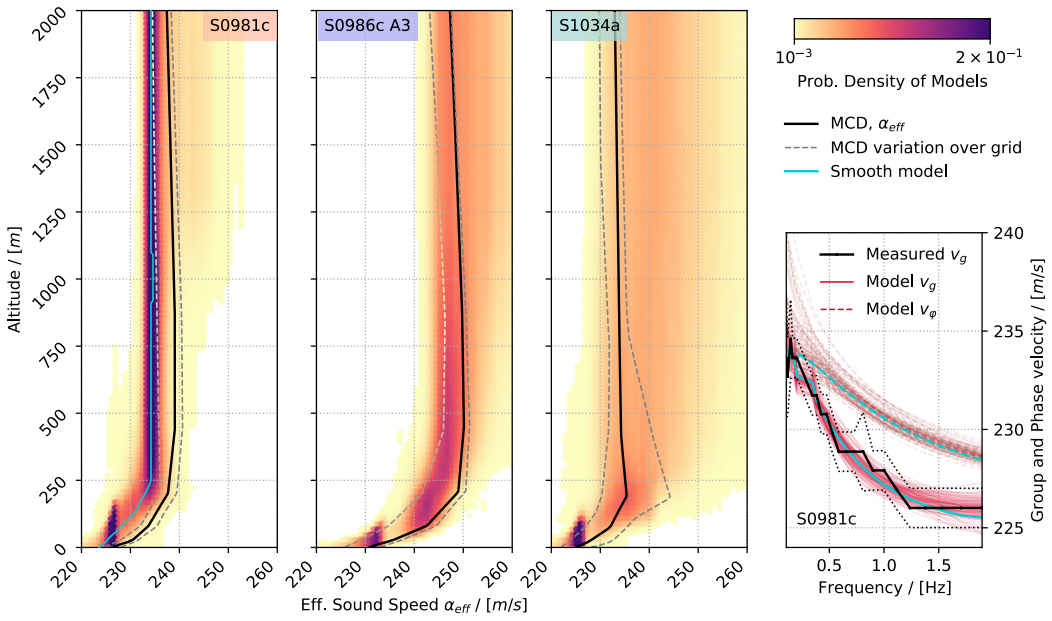

Figure 2. PDFs of the posterior distribution of effective sound speed profiles $\alpha_{\text{eff}}(z)$ inverted for events S0981c, S0986c and S1034a. The MCD profile at InSight location and its spatial variability over the scale of a GCM grid cell is shown with plain and dashed black lines for comparison. The group velocity measurements for S0981c is shown on the right with its uncertainty, together with the group and phase velocities (plain red and dashed brown lines, respectively) estimated from 100 atmosphere models randomly chosen among the posterior distribution.

For event S1034a, we observe that the inverted PDF fits the range of effective sound speed of the MCD. For S0986c, the maximum of the posterior distribution is generally lower than the MCD estimate at InSight location and at the time of the event, but remains within the range of possible variations up to about 1 km altitude, above which the distribution of α_{eff} is less constrained. On the contrary, the PDF of S0981c is constrained within ± 4 m/s from the bottom layer to 2000 m altitude. Although values of α_{eff} agree with the MCD at the surface level, they are lower than the variability range by about ± 2 m/s at high altitudes.

5.2 Estimation of wind

We have focused so far on the effective sound speed, which sums the contribution of local winds to the thermodynamical sound speed, α_{T}, itself a function of temperature. At nighttime on Mars, temperature is driven by thermal radiation of the surface and air, and the MCD yields smooth and predictable profiles for each event (see SI, Fig. S10). On the other hand, winds can be influenced by topography (slope winds or jets) (Savijärvi & Siili, 1993), shear-driven turbulences as well as gravity waves at InSight location (Banfield et al., 2020; Onodera et al., 2024). We also note that there exists more measurements of temperature in the PBL (Seiff & Kirk, 1977; Hinson et al., 1999; Smith et al., 2006; Spiga et al., 2021) than winds (Paton et al., 2021, 2024). This complexity of wind mechanisms and lack of observations suggests that at a specific time of day, temperatures are likely better predicted by climate models than winds. This implies winds could be driving fluctuations in effective sound speed along the source→receiver path.

We propose to estimate wind profiles along this path from posterior models of α_{eff}. To this aim, based on the above argument, we consider that the temperature profiles, and thus the thermodynamical sound speed profiles calculated by the MCD are exact. The wind PDF can then be expressed as:

$$w_{\text{baz, est.}} = \alpha_{\text{eff, McMC}} - \alpha_{\text{T, MCD}}. \tag{2}$$

To calculate this new distribution, we first obtain a MCD profile of α_{T} with the same number of points as the McMC models by extracting only the values measured at the bottom of each layer, $\{\alpha_{\text{T}}(z_n)\}$. The new PDF is shown on Fig. 3. The estimated wind reaches a near zero value at the surface for each event, as expected from surface friction. We find a good agreement between the estimated PDF and the MCD range of wind velocities for S0986c

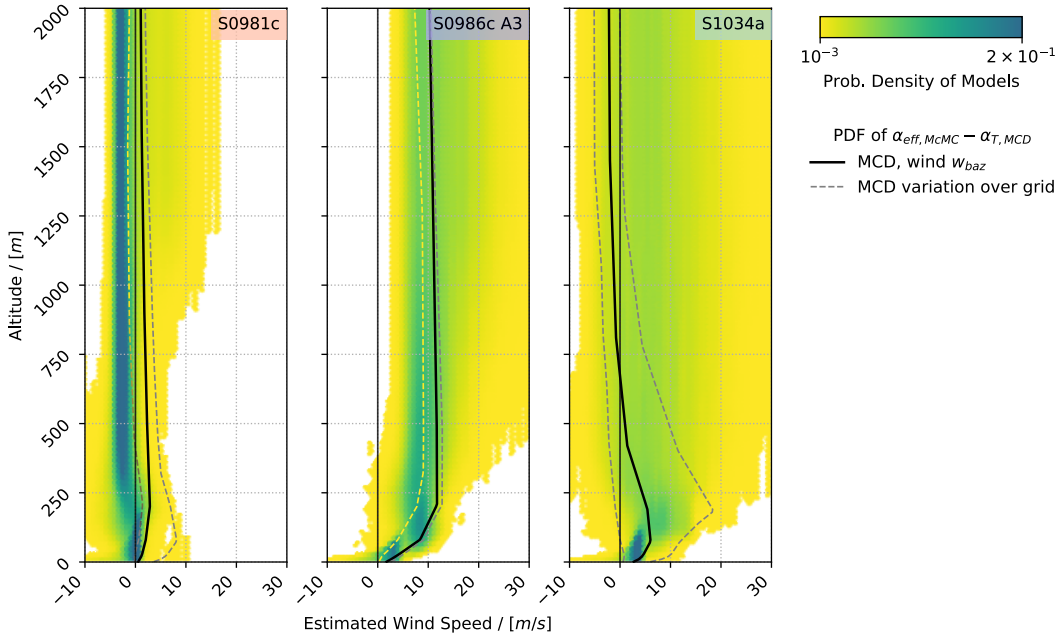

Figure 3. PDFs of the posterior distribution of wind speed profiles estimated for S0981c, S0986c and S1034a in the azimuth of each impact. These distributions are not a direct result of the inversion, but are instead obtained by considering that the temperature and thermodynamic sound speed profiles given by MCD are exact. Consequently, wind speed is estimated from $w_{\mathrm{PDF}}(z) = \alpha_{\mathrm{eff}}(z) - \alpha_{\mathrm{T,\ MCD}}$. The MCD wind profile in the event→receiver azimuth and its variability over a GCM grid cell is shown with plain and dashed black lines.

and S1034a up to 500m altitude. For S0981c, both solutions yield low absolute wind values (< 5 m/s), but they have opposite directions above 250 m altitude. Again, the region of high probability in the estimated PDF is outside the range delimited by the dashed lines, i.e., they do not match values permitted by the MCD interpolation grid.

6 Discussion

The inversion of S0981c yields an ensemble of atmospheric model valid above 500 m, with ±4 m/s sound speed uncertainty. This is surprising as its source is the most distant (240.6 km from InSight) and it has a low signal-to-noise ratio in Fig. 1. Despite the long propagation distance causing high-frequency signal attenuation, S0981c has more group velocity data points at low-frequency compared to S0986c and S1034a. These low-frequencies help constrain atmospheric structures with larger wavelengths, including higher altitudes.

The results also show differences between the inverted PDFs of effective sound speed and the MCD predictions for event S0981c, with lower values of α_{eff} above 500 m altitude. These differences might be due to an atmospheric phenomenon that cannot be captured at the scale of GCM simulations. Assuming temperature is less variable than wind near InSight at night, estimated wind profiles (Fig. 3) indicate that a small $\sim$ 2 m/s wind difference above 500 m altitude can explain the discrepancy in α_{eff}. Notably, winds in the event→receiver direction are lowest for S0981c. At 200 m altitude, the true wind blows from East to West at around 10 m/s (see SI, Fig. S9), while the crater lies directly south of InSight. Thus, an atmospheric phenomenon causing a slight shift in South-North winds could result in a negative amplitude in the event→receiver direction without altering the predicted dominant East→West flow.

Gravity waves, among other phenomena, can cause wind perturbations. Banfield et al. (2020) report examples of gravity waves detected by the APSS pressure sensor, with horizontal wavelength of 30 km and associated wind perturbation of 1 to 2 m/s. Recently, Onodera et al. (2024) claimed the detection of multiple gravity wave signals with high correlation between the pressure sensor and seismometer of InSight. A significant portion of the reported events occur at sunset, between 20h and 0h LMST, a window matching the time of event S0981c. The authors also identify a family of gravity wave events originating from 0 to 30◦ of azimuth. If it were to occur on sol 981, such gravity wave could generate a wind perturbation comparable to the mismatch of the PDF and MCD models. This hypothesis remains unfortunately challenging to test, as the pressure sensors were off at this stage of the mission, and the low frequency seismic data is heavily contaminated by glitches on sol 981.

7 Conclusion

Impact-generated infrasound were recorded for the first time on Mars by the seismometers of the InSight lander. Here, we use this unique dataset to probe the Martian Planetary Boundary Layer. In this region, winds and temperature define the profile of effective sound speed, and control the propagation of infrasound waves.

We invert the effective sound speed in the first two kilometers of the Martian atmosphere using the infrasound group velocity measured for events S0981c, S0986c and S1034a. The inversion confirms the presence of a waveguide in the first $\sim$ 500 m above the surface, where

α_{eff} is increasing with altitude. Inversion results constrain the atmosphere mostly below 500 m altitude. Profiles inverted from events S0986c and S1034a agree with the outputs of the Mars Climate Database. Hence, we validate the calculation of effective sound speed by the MCD in the lower atmosphere of Mars for these two events.

The profile of α_{eff} inverted from event S0981c shows a ~ 2 m/s mismatch to the climate models at high altitude. We show that a wind variation of about 2 m/s, opposed to the infrasound propagation direction, can explain this difference. Wind fluctuations of such amplitude can be caused by many transient and local phenomena (gravity waves, turbulence), which are not resolved at the scale of the MCD. Therefore, results of S0981c do not invalidate the MCD outputs but suggest a need for further investigation of nighttime wind perturbations on Mars.

Acknowledgments

This article is InSight Contribution Number 265 and LA-UR-23-33646. The authors acknowledge NASA, CNES, their partner agencies and institutions (UKSA, SSO, DLR, JPL, IPGP-CNRS, ETHZ, IC, and MPS-MPG) and the flight operations team at JPL, SISMOC, MSDS, IRIS-DMC, and PDS for providing the SEED SEIS data. Authors received financial support from CNES, ANR MAGIS (ANR-19-CE31-0008-08), the Initiative d'Excellence (IdEx) Université Paris Cité (ANR-18-IDEX-0001), The Center for Earth of Space Science (CSES) of LANL, as well as the Research Council of Norway (AIR project, 335903).

Open Research

Data from the SEIS instrument of the InSight mission is available from the SEIS data service (InSight Mars SEIS Data Service, 2019b, 2019a). The Mars Climate Database version 5.3 and above can be downloaded from https://www-mars.lmd.jussieu.fr/.

References

Aki, K., & Richards, P. G. (2002). Quantitative Seismology, 2nd Ed. *Quantitative Seismology, 2nd Ed., by Keiiti Aki and Paul G. Richards. Published by University Science Books, ISBN 0-935702-96-2, 704pp, 2002.*.

Banerdt, W. B., Smrekar, S. E., Banfield, D., Giardini, D., Golombek, M., Johnson, C. L., ... Wieczorek, M. (2020, March). Initial results from the InSight mission on Mars. *Nature Geoscience*, *13*(3), 183–189. doi: 10.1038/s41561-020-0544-y

Banfield, D., Rodriguez-Manfredi, J. A., Russell, C. T., Rowe, K. M., Leneman, D., Lai, H. R., ... The TWINS Team (2018, December). InSight Auxiliary Payload Sensor Suite (APSS). *Space Science Reviews*, *215*(1), 4. doi: 10.1007/s11214-018-0570-x

Banfield, D., Spiga, A., Newman, C., Forget, F., Lemmon, M., Lorenz, R., ... Banerdt, W. B. (2020, March). The atmosphere of Mars as observed by InSight. *Nature Geoscience*, *13*(3), 190–198. doi: 10.1038/s41561-020-0534-0

Ben-Menahem, A., & Singh, S. J. (2012). *Seismic waves and sources*. Springer Science & Business Media.

Ceylan, S., Clinton, J. F., Giardini, D., Stähler, S. C., Horleston, A., Kawamura, T., ... Banerdt, W. B. (2022, December). The marsquake catalogue from InSight, sols 0–1011. *Physics of the Earth and Planetary Interiors*, *333*, 106943. doi: 10.1016/j.pepi.2022.106943

Daubar, I., Lognonné, P., Teanby, N. A., Miljkovic, K., Stevanović, J., Vaubaillon, J., ... Banerdt, W. B. (2018, December). Impact-Seismic Investigations of the InSight Mission. , *214*(8), 132. doi: 10.1007/s11214-018-0562-x

Daubar, I. J., Fernando, B. A., Garcia, R. F., Grindrod, P. M., Zenhäusern, G., Wójcicka, N., ... Banerdt, W. B. (2023, September). Two Seismic Events from InSight Confirmed as New Impacts on Mars. *The Planetary Science Journal*, *4*(9), 175. doi: 10.3847/PSJ/ace9b4

Forget, F., Hourdin, F., Fournier, R., Hourdin, C., Talagrand, O., Collins, M., ... Huot, J.-P. (1999, October). Improved general circulation models of the Martian atmosphere from the surface to above 80 km. *Journal of Geophysical Research*, *104*, 24155–24176. doi: 10.1029/1999JE001025

Forget, F., Millour, E., Spiga, A., Madeleine, J.-B., Pottier, A., Navarro, T., ... Read, P. L. (2014, January). Simulating the Mars Climate with the LMD Mars Global Climate Model: Validation and issues. In F. Forget & M. Millour (Eds.), *The Fifth International Workshop on the Mars Atmosphere: Modelling and Observations* (p. id.1204). Oxford, United Kingdom.

Forget, F., Wanherdrick, Y., & Lewis, S. R. (2001). *Validation of the Mars General Circulation Model and Climate Database with new spacecraft observations* (Tech. Note for ESA Contract 11369/95/NL/JG).

Garcia, R. F., Brissaud, Q., Rolland, L., Martin, R., Komatitsch, D., Spiga, A., ... Banerdt, B. (2017, October). Finite-Difference Modeling of Acoustic and Gravity Wave Propa-

gation in Mars Atmosphere: Application to Infrasounds Emitted by Meteor Impacts. *Space Science Reviews*, *211*(1), 547–570. doi: 10.1007/s11214-016-0324-6

Garcia, R. F., Daubar, I. J., Beucler, É., Posiolova, L. V., Collins, G. S., Lognonné, P., ... Banerdt, W. B. (2022, September). Newly formed craters on Mars located using seismic and acoustic wave data from InSight. *Nature Geoscience*, 1–7. doi: 10.1038/s41561-022-01014-0

Gaudot, I., Beucler, É., Mocquet, A., Drilleau, M., Haugmard, M., Bonnin, M., ... Leparoux, D. (2021, March). 3-D crustal VS model of western France and the surrounding regions using Monte Carlo inversion of seismic noise cross-correlation dispersion diagrams. *Geophysical Journal International*, *224*(3), 2173–2188. doi: 10.1093/gji/ggaa552

Geyer, C. J. (1991). Markov Chain Monte Carlo Maximum Likelihood. In *Computing Science and Statistics: Proceedings of the 23rd Symposium on the Interface* (pp. 156–163). New York: American Statistical Association.

Herrin, E. T., Kim, T. S., & Stump, B. W. (2006). Evidence for an infrasound waveguide. *Geophysical Research Letters*, *33*(7). (_eprint: https://onlinelibrary.wiley.com/doi/pdf/10.1029/2005GL025491) doi: 10.1029/2005GL025491

Hinson, D. P., Simpson, R. A., Twicken, J. D., Tyler, G. L., & Flasar, F. M. (1999). Initial results from radio occultation measurements with Mars Global Surveyor. *Journal of Geophysical Research: Planets*, *104*(E11), 26997–27012. doi: 10.1029/1999JE001069

InSight Mars SEIS Data Service. (2019a). *Data Service, InSight SEIS Data Bundle.* PDS Geosciences (GEO) Node. doi: 10.17189/1517570

InSight Mars SEIS Data Service. (2019b). *SEIS raw data, Insight Mission.* IPGP, JPL, CNES, ETHZ, ICL, MPS, ISAE-Supaero, LPG, MFSC. doi: 10.18715/SEIS.INSIGHT.XB_2016

InSight Marsquake Service. (2023). *Mars seismic catalogue, insight mission; v14 2023-04-01.* ETHZ, IPGP, JPL, ICL, Univ. Bristol. Retrieved from https://www.insight.ethz.ch/seismicity/catalog/v14 doi: 10.12686/a21

Lognonné, P., Banerdt, W. B., Giardini, D., Pike, W. T., Christensen, U., Laudet, P., ... Wookey, J. (2019). SEIS: Insight's Seismic Experiment for Internal Structure of Mars. *Space Science Reviews*, *215*(1), 12. doi: 10.1007/s11214-018-0574-6

Martire, L., Garcia, R. F., Rolland, L., Spiga, A., Lognonné, P. H., Banfield, D., ... Mar-

tin, R. (2020). Martian Infrasound: Numerical Modeling and Analysis of InSight's Data. *Journal of Geophysical Research: Planets*, *125*(6), e2020JE006376. (_eprint: https://agupubs.onlinelibrary.wiley.com/doi/pdf/10.1029/2020JE006376) doi: 10.1029/2020JE006376

Mason, E. L., & Smith, M. D. (2021, May). Temperature fluctuations and boundary layer turbulence as seen by Mars Exploration Rovers Miniature Thermal Emission Spectrometer. *Icarus*, *360*, 114350. doi: 10.1016/j.icarus.2021.114350

Millour, E., Forget, F., Spiga, A., Navarro, T., Madeleine, J. B., Montabone, L., ... MCD/GCM development Team (2015, October). The Mars Climate Database (MCD version 5.2). In *European Planetary Science Congress 2015* (Vol. EPSC2015, p. 438). Nantes, France.

Millour, E., Forget, F., Spiga, A., Vals, M., Zakharov, V., Montabone, L., ... Read, P. L. (2018). The Mars Climate Database (Version 5.3). In *Scientific Workshop: "From Mars Express to ExoMars"*. ESAC Madrid, Spain.

Moudden, Y., & McConnell, J. C. (2005). A new model for multiscale modeling of the Martian atmosphere, GM3. *Journal of Geophysical Research: Planets*, *110*(E4). doi: 10.1029/2004JE002354

Negraru, P. T., & Herrin, E. T. (2009, July). On Infrasound Waveguides and Dispersion. *Seismological Research Letters*, *80*(4), 565–571. doi: 10.1785/gssrl.80.4.565

Onodera, K., Nishida, K., Widmer-Schnidrig, R., Kawamura, T., Spiga, A., Hernandez-Bernal, J., ... Murdoch, N. (2024, March). Seismic Detection of Atmospheric Gravity Waves on Mars. , *3040*, 1121.

Paton, M. D., Leino, J., Harri, A. M., & Savijärvi, H. (2021, October). Martian boundary layer wind profiles during the landings of Viking and InSight. *Icarus*, *367*, 114581. doi: 10.1016/j.icarus.2021.114581

Paton, M. D., Savijärvi, H., Harri, A. M., Leino, J., Bertrand, T., Viúdez-Moreiras, D., ... Newman, C. (2024, June). Inferred wind speed and direction during the descent and landing of Perseverance on Mars. *Icarus*, *415*, 116045. doi: 10.1016/j.icarus.2024.116045

Petrosyan, A., Galperin, B., Larsen, S. E., Lewis, S. R., Määttänen, A., Read, P. L., ... Vázquez, L. (2011). The Martian Atmospheric Boundary Layer. *Reviews of Geophysics*, *49*(3). doi: 10.1029/2010RG000351

Sambridge, M. (2014, January). A Parallel Tempering algorithm for probabilistic sampling

and multimodal optimization. *Geophysical Journal International*, *196*(1), 357–374. doi: 10.1093/gji/ggt342

Savijärvi, H., & Siili, T. (1993, January). The Martian Slope Winds and the Nocturnal PBL Jet. *Journal of the Atmospheric Sciences*, *50*(1), 77–88. doi: 10.1175/1520-0469(1993)050⟨0077:TMSWAT⟩2.0.CO;2

Schneider, F. M., Fuchs, F., Kolínský, P., Caffagni, E., Serafin, S., Dorninger, M., & Bokelmann, G. (2018, November). Seismo-acoustic signals of the Baumgarten (Austria) gas explosion detected by the AlpArray seismic network. *Earth and Planetary Science Letters*, *502*, 104–114. doi: 10.1016/j.epsl.2018.08.034

Segschneider, J., Grieger, B., Keller, H. U., Lunkeit, F., Kirk, E., Fraedrich, K., ... Greve, R. (2005, May). Response of the intermediate complexity Mars Climate Simulator to different obliquity angles. *Planetary and Space Science*, *53*(6), 659–670. doi: 10.1016/j.pss.2004.10.003

Seiff, A., & Kirk, D. B. (1977). Structure of the atmosphere of Mars in summer at mid-latitudes. *Journal of Geophysical Research (1896-1977)*, *82*(28), 4364–4378. doi: 10.1029/JS082i028p04364

Smith, M. D., Wolff, M. J., Spanovich, N., Ghosh, A., Banfield, D., Christensen, P. R., ... Squyres, S. W. (2006). One Martian year of atmospheric observations using MER Mini-TES. *Journal of Geophysical Research: Planets*, *111*(E12). doi: 10.1029/2006JE002770

Sorrells, G. G. (1971). A preliminary investigation into the relationship between long-period seismic noise and local fluctuations in the atmospheric pressure field. *Geophysical Journal International*, *26*(1-4), 71–82.

Spiga, A., Murdoch, N., Lorenz, R., Forget, F., Newman, C., Rodriguez, S., ... Banerdt, W. B. (2021). A Study of Daytime Convective Vortices and Turbulence in the Martian Planetary Boundary Layer Based on Half-a-Year of InSight Atmospheric Measurements and Large-Eddy Simulations. *Journal of Geophysical Research: Planets*, *126*(1), e2020JE006511. doi: 10.1029/2020JE006511

Takahashi, Y. O., Fujiwara, H., & Fukunishi, H. (2006). Vertical and latitudinal structure of the migrating diurnal tide in the Martian atmosphere: Numerical investigations. *Journal of Geophysical Research: Planets*, *111*(E1). doi: 10.1029/2005JE002543

Tanimoto, T., & Wang, J. (2019). Theory for deriving shallow elasticity structure from colocated seismic and pressure data. *Journal of Geophysical Research: Solid Earth*,

124(6), 5811–5835.

Xu, Z., Froment, M., Garcia, R. F., Beucler, É., Onodera, K., Kawamura, T., ... Banerdt, W. B. (2022). Modeling Seismic Recordings of High-Frequency Guided Infrasound on Mars. *Journal of Geophysical Research: Planets*, *127*(11), e2022JE007483. doi: 10.1029/2022JE007483

Xu, Z., & Lognonné, P. (2024). A comprehensive theory for 1D (an)elastic medium deformation due to plane-wave fluid pressure perturbation. *Geophysical Journal International*, *236*(3), 1499-1512. doi: 10.1093/gji/ggae005